Supplementary Information (SI) for Journal of Materials Chemistry A.

Supporting Information for

Lithium extraction from low-grade brines via strain-induced electronic structure modulation of MnO_2 nanorods by Mg Incorporation

Yang Bao [a,b,c,1], *YunJia Ling* [a,b,c,1], *ZeYing Ji* [a,b], *Hongru Zhou* [a,b], *Shaoxian Song* [a,b,d], *Feifei Jia* [a,b,*], *Jianbo Li* [a,b,**], *Mildred Quintana* [c]

[a] Key Laboratory of Green Utilization of Critical Non-metallic Mineral Resources of Ministry of Education, Wuhan University of Technology, Wuhan 430070, Hubei, China

[b] School of Resources and Environmental Engineering, Wuhan University of Technology, Wuhan 430070, Hubei, China

[c] Facultad de Ciencias y Centro de Investigación en Ciencias de La Salud y Biomedicina (CICSAB), Universidad Autónoma de San Luis Potosí, Av. Sierra Leona 550, San Luis Potosí, S.L.P. 78210, México

[d] Instituto de Metalurgia, Universidad Autónoma de San Luis Potosí, Av. Sierra Leona 550, San Luis Potosí 78210, Mexico

[1]These authors contribute equally to this work.

* Corresponding author.

E-mail address: feifeijia@whut.edu.cn (**FF Jia**)

E-mail address: lijianbo3051@163.com (**JB Li**)

Number of Pages:	**33**
Number of Texts:	**2**
Number of Tables:	**8**
Number of Figures:	**18**
Number of References:	**13**

Text S1. Detailed Electrochemical Characterizations

The CV analyses were carried out at scan rates from 2 to 20 mV s^{-1} within a potential window of 0.2 to 1.2 V for MnO_2 and FLA-MnO_2 electrodes in 1 M LiCl, NaCl, KCl, $MgCl_2$ and $CaCl_2$ solutions. A series of CV measurements were carried out at different scan rates in order to examine the capacitive contribution. The specific capacitance can be calculated according to the following eq. S1:

$$C_S = \frac{\int IdV}{2mv\Delta V} \tag{S1}$$

Where $\boldsymbol{I}$ is the Response current (A), $\boldsymbol{m}$ is the mass of the electrode materials (g), $\boldsymbol{v}$ refers to the scan rate (mV s^{-1}), and $\boldsymbol{\Delta V}$ is the voltage change excluding IR (current resistance) drop in the discharge process (V).

The Li^+ diffusion behavior of various electrodes was further investigated by analyzing the CV curves at different scanning rates. The Li^+ diffusion coefficients of the electrodes were calculated according to the following Eq. S2:

$$I_p = 2.69 \times 10^5 \times n^{3/2} \times A \times D_{Li^+}^{1/2} \times v^{1/2} \times C_0 \tag{S2}$$

Where $\boldsymbol{I_p}$ is the peak current (A), $\boldsymbol{v}$ refers to the scan rate (V s^{-1}), $\boldsymbol{n}$ is the charge transfer number. $\boldsymbol{A}$ is the electrode surface area (cm^2), $\boldsymbol{D_{Li+}}$ represents the Li^+ diffusion coefficient (cm^2 s^{-1}), $\boldsymbol{C_0}$ is the bulk concentration of Li^+ (mol cm^{-3}), respectively. The relationship between $\boldsymbol{I_p}$ and $\boldsymbol{v^{1/2}}$ is presented in Fig. S1. According to the slopes of $\boldsymbol{I_p}$ vs $\boldsymbol{v^{1/2}}$ plots, the $\boldsymbol{D_{Li+}}$ were calculated and listed in Table S3.

The current response at a given potential can be defined by the combination of the diffusion-controlled (faradaic intercalation) and outer charge (capacitive contribution) process. This can be stated by the following eq. S3 & eq. S4:

$$i = av^b \tag{S3}$$

$$\log i = b\log v + \log a \tag{S4}$$

Where $\boldsymbol{i}$ is the peak current (A g^{-1}), $\boldsymbol{v}$ refers to the scan rate (mV s^{-1}), $\boldsymbol{a}$ and $\boldsymbol{b}$ are parameters obtained after linear fitting. When the b value is close to 0.5, it indicates a diffusion-controlled battery behavior, when the b value is close to 1, it represents the outer charge capacitive behavior.[1]

The specific capacitance of an electrode material is often determined by both diffusion-controlled specific capacitance and capacitance-controlled specific capacitance, which obeys the following eq. S5 & eq. S6:

$$i(V) = k_1 v + k_2 v^{1/2} \tag{S5}$$

$$\frac{i(V)}{v^{1/2}} = k_1 v^{1/2} + k_2 \tag{S6}$$

Where $\boldsymbol{i}$ is the peak current (A g^{-1}), $\boldsymbol{v}$ refers to the scan rate (mV s^{-1}), $\boldsymbol{k_1}$ and $\boldsymbol{k_2}$ are contribution rate. $\boldsymbol{k_1 v}$ and $\boldsymbol{k_2 v^{1/2}}$ correspond to the capacitance-controlled and the diffusion-controlled contributions, respectively.[2]

The GCD experiments were performed at specific currents of 2 to 12.0 A g^{-1} within the same potential windows. Specific capacitance is calculated from the discharge curve after the IR drop using eq. S7 given below,

$$C_S = \frac{I \times \Delta t}{m \times \Delta V} \tag{S7}$$

where $\boldsymbol{C_s}$ is the specific capacitance (F g^{-1}), $\boldsymbol{I}$ refer to the response current (A), $\boldsymbol{\Delta t}$ is the discharge time (s), $\boldsymbol{m}$ is the mass of the electrode materials (g), and $\Delta \boldsymbol{V}$ is the voltage change excluding IR (current resistance) drop in the discharge process (V).

The EIS data were collected in the frequency range from 100 kHz to 10 mHz, and the applied bias voltage and ac amplitude were set at open-circuit potential and 5.0 mV. The EIS plots consist of semicircles in the high-frequency region and nearly straight lines in the low-frequency region. In general, the diameter of the semicircle represents the charge transfer resistance ($\boldsymbol{R_{ct}}$) caused by the redox reaction at the electrode/electrolyte interface, and the slope of the straight line represents the Warburg impedance ($\boldsymbol{Z_w}$) caused by the migration of interface ions from the electrolyte to the electrode. The equivalent series resistance ($\boldsymbol{R}_s$) can be obtained from the intercept of the semicircle at the real axis ($\boldsymbol{Z'}$) and used to assess the electrical conductivity of the electrodes.[3] All the EIS data were fitted using the Zview software (version 2.80, Scribner Associates Inc.) and the best-fitting parameters are tabulated in Table S2.

Text S2. Detailed Electrode Fabrication and HCDI Tests

The working electrodes were fabricated by combining MnO_2 or FLA-MnO_2, acetylene black (Alfa Aesar, Shanghai, China), and polyvinylidene fluoride (PVDF, Aladdin Chemical Co.) in an 8:1:1 ratio. The mixture was ground by hand and then dispersed in 1-methyl-2-pyrrolidone at a ratio of PVDF to 1-methyl-2-pyrrolidone of 0.1 g:8 ml, which then was deposited onto a graphite paper with a size of 5 cm × 5 cm and dried in oven at 70 °C for 12 h. A total mass of 30 mg of the above mixture was applied for each electrode. The AC electrodes were prepared following the same method as above for preparing the working electrodes. As shown in Fig. 1, the HCDI cell consisted of MnO_2 or FLA-MnO_2 electrodes (as positive), activated carbon electrode (AC, as negative), anion-exchange membrane (AEM). The 0.8 mm thick silicon gasket placed between the anode and cathode as the feed chamber (~ 2 mL), and the AEM is sandwiched between the chamber and the AC electrode.

In the electrochemical lithium recovery experiments, all the experiments were conducted in batch mode and carried out under constant voltage conditions, 40 mL feed solution was circulated through the HCDI cell, at a flow rate of 40 mL min^{-1}, the duration of each desalination cycle is 80 min, which is divided into the charging process and discharging process. The conductivity of effluent was consecutively monitored by a DDSJ-307F conductivity meter (INESA Scientific Instrument Co., Shanghai, China. The standard curve was obtained from the linear relationship between conductivity and concentration. The ***Adsorption capacity*** (SAC, mg g^{-1}) and ***Adsorption ratio*** (%) were calculated according to eq. S8 & eq. S9:

$$SAC = \frac{(C_0 - C_e)V}{m} \tag{S8}$$

$$Adsorption\,ratio = \frac{(C_0 - C_e)}{C_0} \times 100 \tag{S9}$$

where C_0 (mg L^{-1}) and C_e (mg L^{-1}) represent the initial and final concentration of the Li-ion solution, respectively. V (L) is the volume of the solution, and m (g) is the mass of the active material.

The ***Charge efficiency*** (Λ) was used as another metric for evaluation of the HCDI performance, as given in eq. S10,

$$\wedge = \frac{SAC \times F}{\sum}$$

(S10)

where $\boldsymbol{F}$ is the Faraday constant (96485 C mol^{-1}), $\sum$ (charge, C·g^{-1}) is obtained by integrating the corresponding current.

The ***Faradaic efficiency*** (***FE***) was used as another metric for evaluation of the HCDI performance, as given in eq. S11,

$$FE = \left(\frac{n(Li^+) \times F}{\sum}\right) \times 100\% \tag{S11}$$

Where ***n(Li⁺)*** is the experimentally measured molar number (mol) of Li^+ ion intercalation, $\boldsymbol{F}$ is the Faraday constant (96485 C mol^{-1}), $\sum$ (charge, C·g^{-1}) is obtained by integrating the corresponding current.

Kim-Yoon plot was also employed to evaluate the HCDI performance. The ***Salt adsorption rate*** (SAR, mg g^{-1} min^{-1}) can be calculated by eq. S12:

$$SAR = \frac{(C_0 - C_t)V}{m \times t} \tag{S12}$$

where $\boldsymbol{C_t}$ (mg L^{-1}) represents the instantaneous concentration of solution at time $\boldsymbol{t}$ (min).

The ***Energy consumption*** (W, Wh g^{-1}) can be calculated by eq. S13:

$$W = \frac{v \times \int idt}{3600 \times (C_0 - C_e) \times V} \tag{S13}$$

where $\boldsymbol{v}$ represents the applied voltage (V), $\boldsymbol{i}$ is the consumed current (A), $\boldsymbol{t}$ is the time (s).

The concentrations of different ions in the binary Mg^{2+}/Li^+ mixed solution and Lop Nor the Xieli salt flats low-grade brine were measured by inductively coupled plasma optical emission spectroscopy (ICP-OES). Various ***Ion separation factors*** ($\alpha^{Li^+}_{M^{n+}}$) (the adsorption ratio of Li^+ to the M^{n+} (Na^+, K^+, Ca^{2+} and Mg^{2+})) can be calculated by eq. S14:

$$\alpha^{Li^+}_{M^{n+}} = \frac{Adsorption\ ratio\ (Li^+)}{Adsorption\ ratio\ (M^{n+})} \tag{S14}$$

The ***Dissolution loss ratio*** of Mn^{2+} from the positive electrodes during the long-term cycles was calculated by the following eq. S15:

$$Dissolution\ loss\ ratio = \frac{C \times V}{m \times w} \tag{S15}$$

where ***C*** (g L^{-1}) is the concentration of Mn^{2+} in the cycling solution (Mn^{2+} concentration was detected by ICP-OES), w (%) is the mass fraction of Mn in MnO_2 or FLA-MnO_2 electrode.[4]

The hydration energy calculations were conducted using the $Dmol^3$ module in Materials Studio software. The energy task was performed with the GGA-PBE (Perdew–Burke–Ernzerh of generalized gradient approximation) exchange-correlation functional, effective core potentials (ECP) for core electron treatment, and the DNP basis set under fine precision settings. The charge states were set to +1 for Li^+, Na^+ and K^+, and +2 for Ca^{2+} and Mg^{2+}, with singlet spin applied to all ions. For the gas-phase energy (E-gas) calculation, the COSMO solvation model was disabled. In contrast, the solvent-phase energy (E-solvent) calculation employed the COSMO implicit solvent model with a dielectric constant of water (ε = 78.54) to simulate aqueous environments.

Table S1

Table S1. ICP results of MnO_2 and FLA-MnO_2.

material	Mass percent (%)		Molar ratio
	Mn	Mg	Mn : Mg
MnO_2	55.367	0	-
FLA-MnO_2	55.597	2.28	1.012:0.094

Table S2

Table S2. IR Drop, Specific Capacitance (***C***$_s$), Best-Fitting Equivalent Series Resistance (***R***$_s$), and Charge-Transfer Resistance (***R***$_{ct}$) of MnO_2 and FLA-MnO_2 Electrodes

material	IR drop [a] (mV)	C_s [a] (F g^{-1})	R_s (Ω)	R_{ct} (Ω)
MnO_2	90.97	356.24	2.52	0.85
FLA-MnO_2	79.8	619.13	2.21	0.64

[a] measured by the GCD discharge curves at a specific current of 2 A g^{-1}.

Table S3

Table S3. Li^+ diffusion coefficients of MnO_2 and FLA-MnO_2 electrodes.

Electrodes	O_{x1} (cm^2 s^{-1})	O_{x2} (cm^2 s^{-1})	R_{ed1} (cm^2 s^{-1})	R_{ed2} (cm^2 s^{-1})
MnO_2	3.82×10^{-11}	7.54×10^{-11}	6.91×10^{-11}	3.54×10^{-11}
FLA-MnO_2	6.75×10^{-11}	1.07×10^{-10}	9.84×10^{-11}	5.22×10^{-11}

Table S4

Table S4. Physical and thermodynamic properties of the ions in this study.[4]

Ions	Diffusion coefficient (10^{-9} m^2 s^{-1})	Ion Radius (nm)	Hydrated Radius (nm)	Hydration free energy (kJ mol^{-1})
Li^+	1.03	0.076	0.382	-515
Na^+	1.33	0.116	0.358	-365
K^+	1.96	0.133	0.331	-271
Ca^{2+}	0.71	0.106	0.412	-1650
Mg^{2+}	0.79	0.072	0.428	-1828

Table S5

Table S5. Chemical composition of Lop Nor the Xieli salt flats low-grade original brine (Xinjiang, China)

Ions	Concentration (mg L^{-1})	Ratio (M/Li^+)
Li^+	42.086	1
Na^+	95366.536	2272.7
K^+	10101.310	244.4
Ca^{2+}	57.710	1.4
Mg^{2+}	29403.096	704.8

The value of Lop Nor the Xieli salt flats low-grade original brine measured: pH 6.1, conductivity 123.1 ms cm^{-1}, TDS 61.5 mg L^{-1}.

Table S6

Table S6. The first column gives the solutions with different Li^+ concentrations prepared in the laboratory, the second column represents the conductivity values of the solutions from the first column, the third column shows the theoretically calculated Li^+ concentration from the first column and the fourth column displays the Li^+ concentrations measured using ICP.

LiCl concentration (mg L^{-1})	**Conductivity (us cm^{-1})**	**Li^+ concentration (mg L^{-1}, Theoretical value)**	**Li^+ concentration (mg L^{-1}, ICP measured)**
4	6.5	0.6549	0.652
5	7.2	0.8186	0.815
10	14.8	1.6372	1.631
20	30.6	3.2745	3.268
50	84.1	8.1863	8.152
100	186.7	16.3726	16.308
200	384.2	32.7452	32.617
500	980.6	81.863	81.562

Table S7

Table S7. Comparison of Li Adsorption Capacity of MnO_2 Based Electrodes Applied for CDI.

Electrodes	Li concentration (mg L^{-1})	Energy consumption (Wh g^{-1})	Retention/ cycles	Adsorption capacity (mg g^{-1})	Manganese dissolution/ cycles	Ref.
λ-MnO_2/rGO-0.2‖AC	212	1.2	--	18	--	[5]
λ-MnO_2‖AC	50	6.83	--	18.1	--	[6]
λ-MnO_2/rGO/Ca-alg	80	--	98.3%/100	32.7	--	[7]
LMO-$Al_{0.05}$‖ PANI/AC	165	0.371	--	21.7	1.9%/100	[4]
LMOns@CC‖AC	200	--	97.4%/10	32.9	0.35%/10	[8]
rGO/LNCM‖AC	164	0.2	--	13.8	--	[9]
Meso-LMO@GF	150	3.34	90.4%/20	26.3	--	[10]
λ-MnO_2‖Pt	4.24	4.71	--	11	--	[11]
LNMMO‖AC	210	1.13	90.8%/30	14.4	--	[12]
$LiMn_2O_4$@carbon fiber	--	2.28	91%/100	12	0.077%/1	[13]
FLA-MnO_2‖AC	32.74	0.45	82%/100	30.1	1.3%/100	This work

Table S8

Table S8. The hydration energies of different ions obtained through computational simulation.

Ions	E_gas (Ha)	E_solvent (Ha)	ΔG_hydration (Ha)	ΔG_hydration (KJ/mol)
Li^+	-7.2570926	-7.4224253	-0.1653327	-424.1610418
Na^+	-161.9757824	-162.1200183	-0.1442359	-370.0372014
K^+	-599.5470456	-599.6639022	-0.1168566	-299.7956073
Ca^{2+}	-199.1117977	-199.7449046	-0.6331069	-1624.235752
Mg^{2+}	-676.6852151	-677.1529253	-0.4677102	-1199.910518

Figure S1

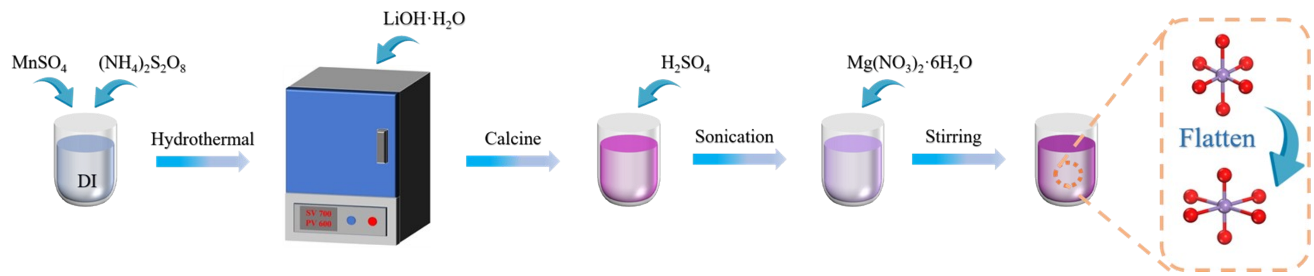

Figure S1. Illustration of the synthesis of FLA-MnO_2.

Figure S2

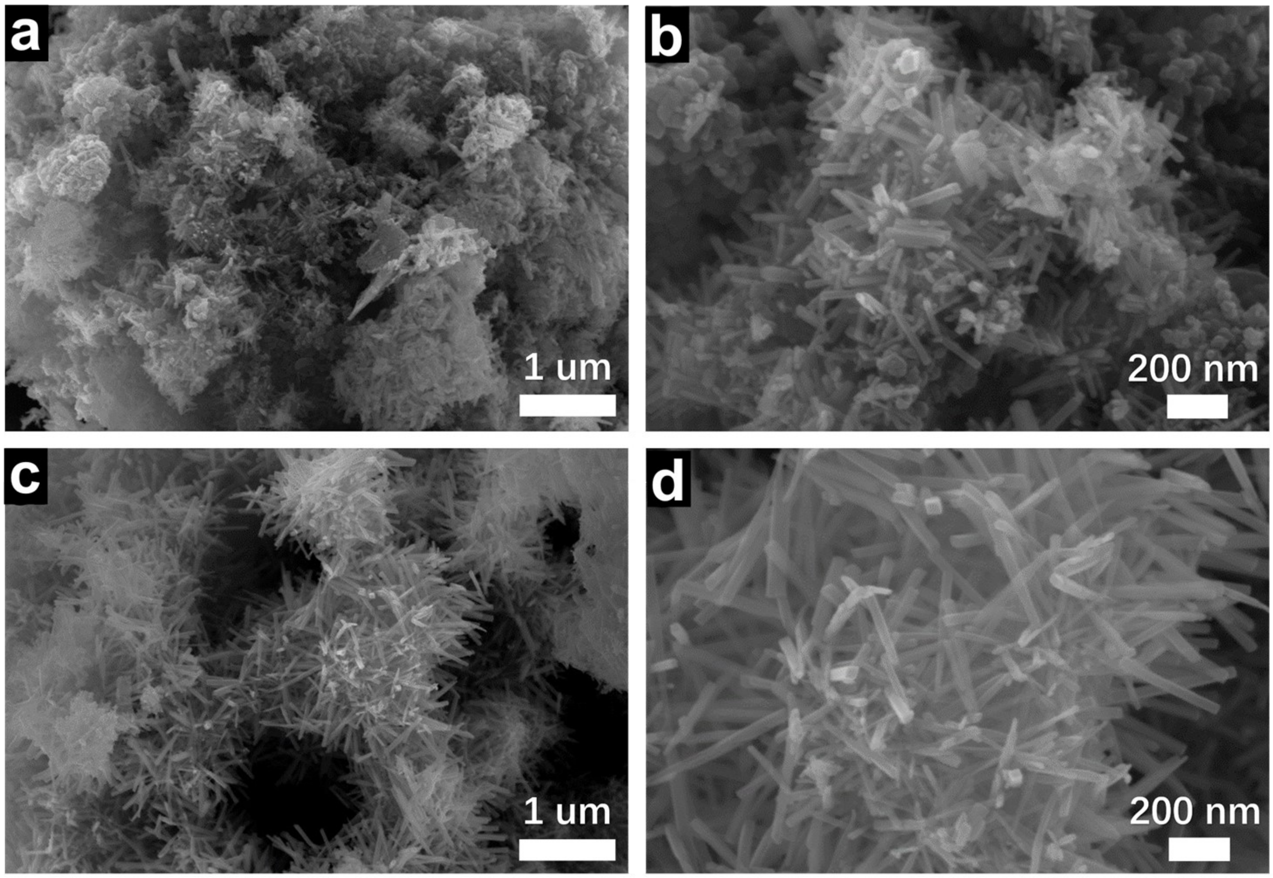

Figure S2. SEM images of (**a, b**) MnO_2, (**c, d**) FLA-MnO_2.

Figure S3

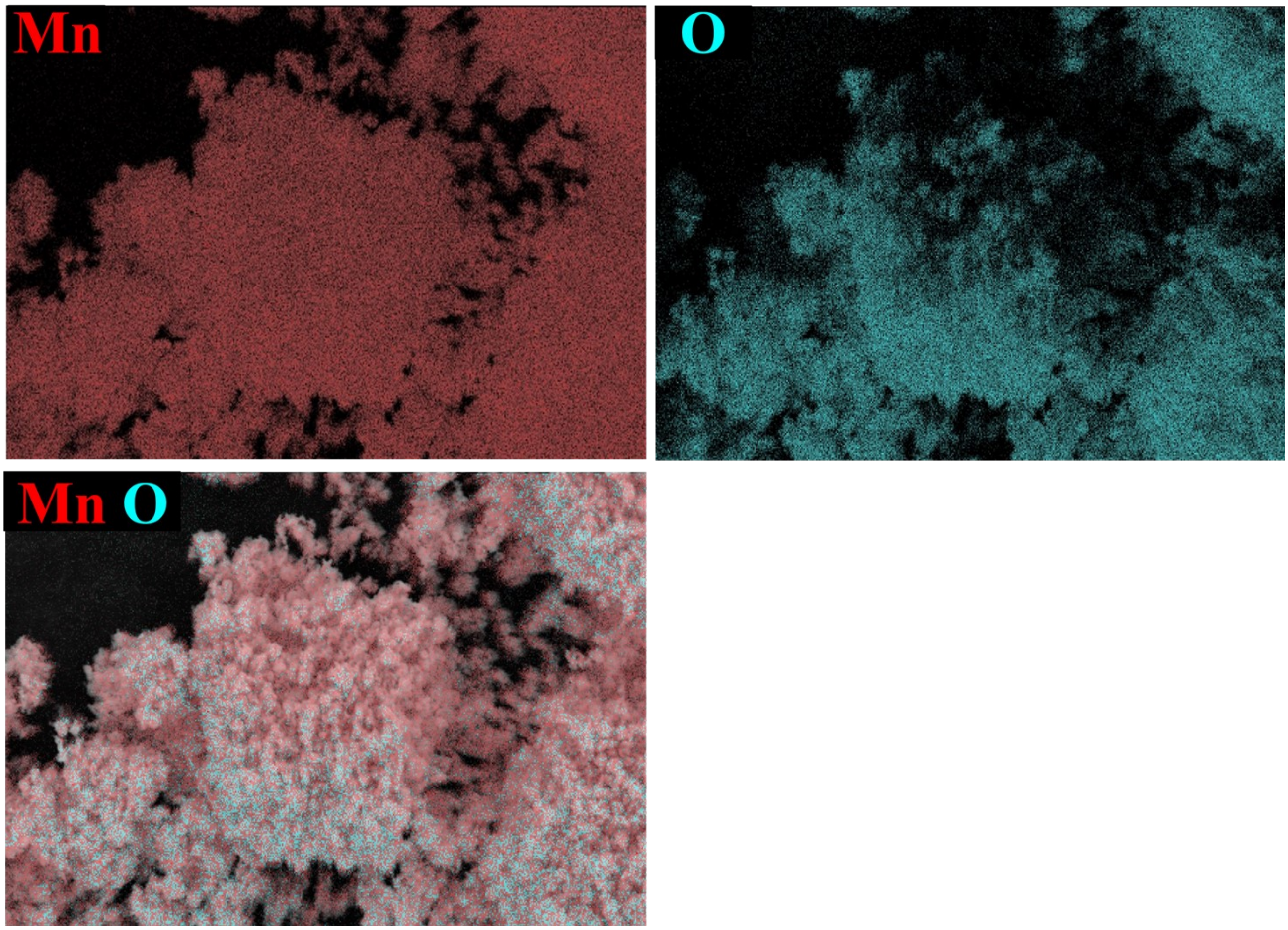

Figure S3. Element mapping of MnO_2.

Figure S4

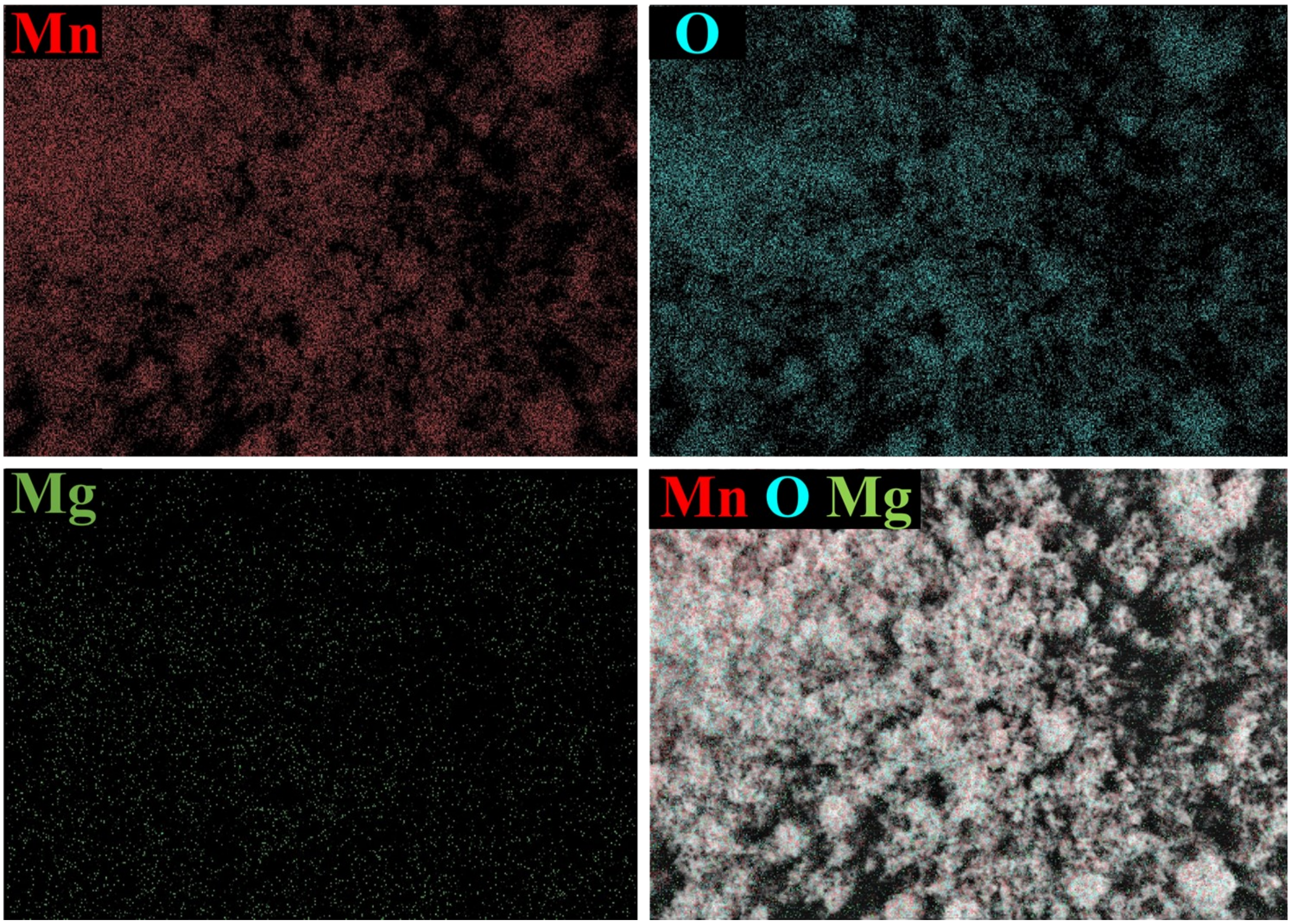

Figure S4. Element mapping of FLA-MnO_2.

Figure S5

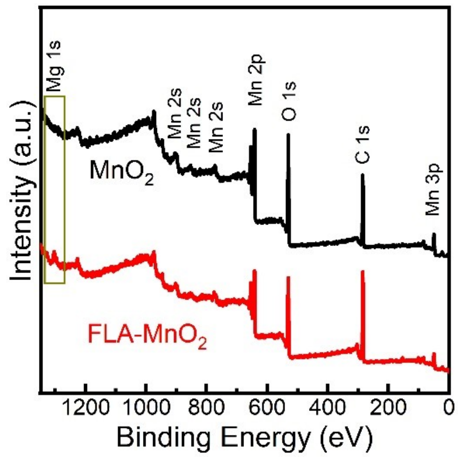

Figure S5. XPS survey of MnO_2 and FLA-MnO_2.

Figure S6

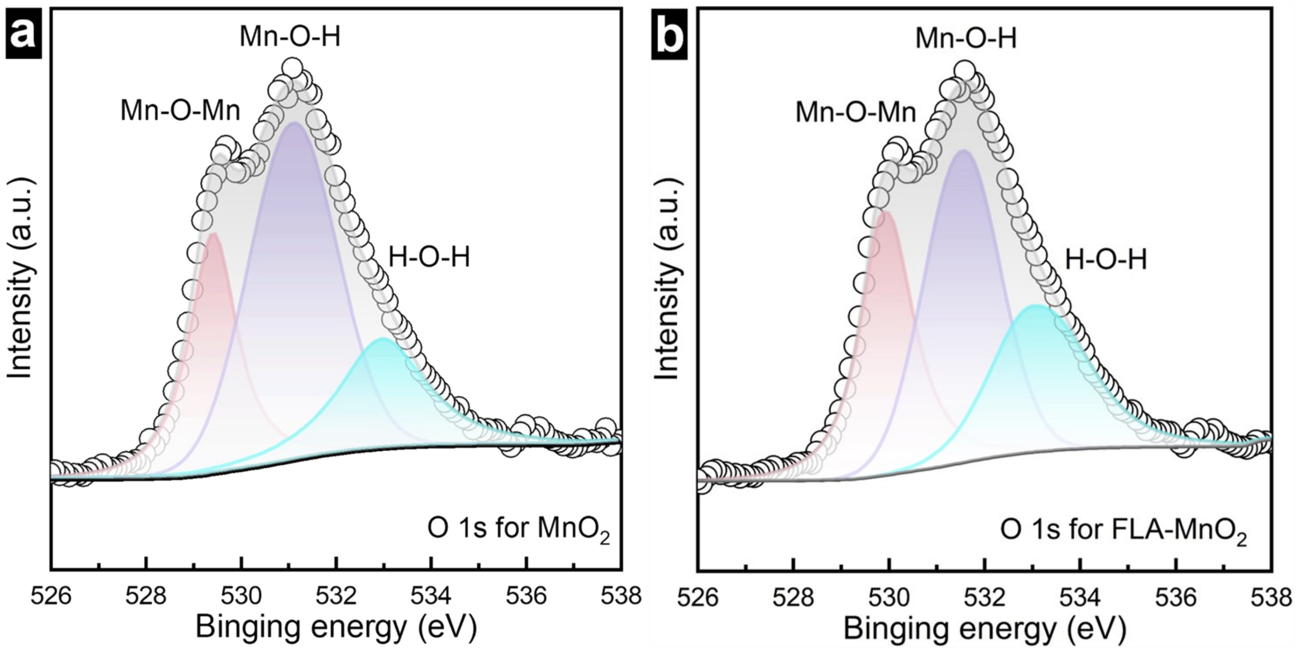

Figure S6. O 1s survey of (**a**) MnO_2, (**b**) FLA-MnO_2.

Figure S7

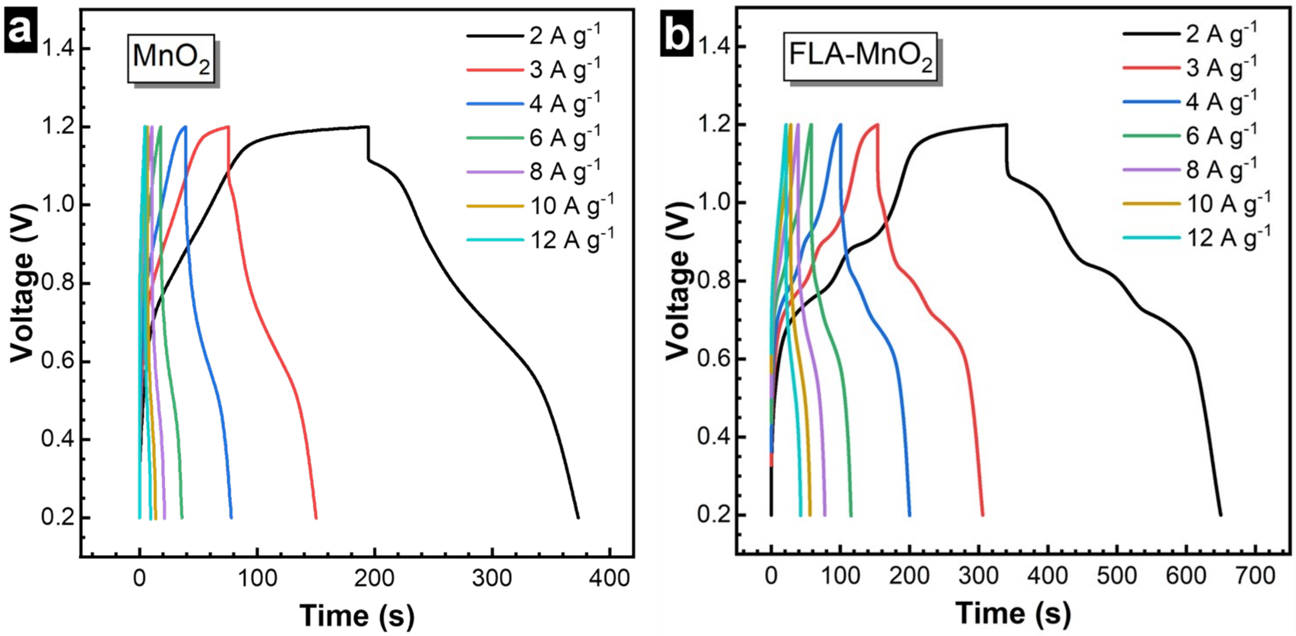

Figure S7. GCD curves of MnO_2 and FLA-MnO_2 electrodes at different specific currents: (**a**) MnO_2, (**b**) FLA-MnO_2,

Figure S8

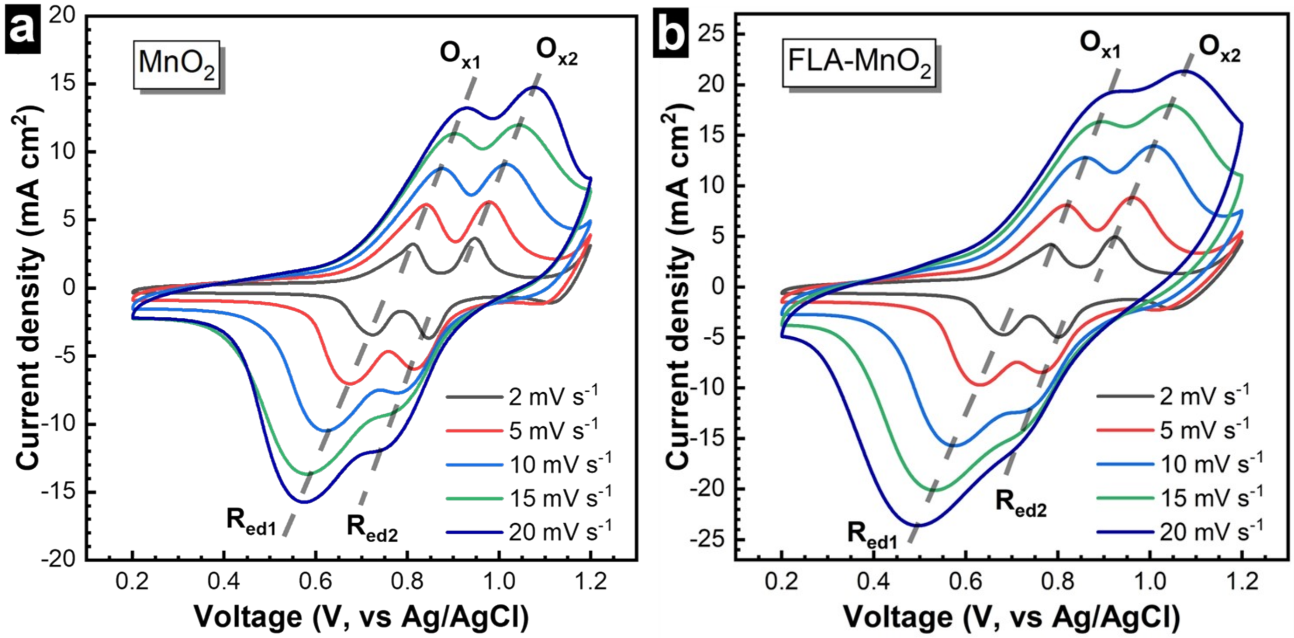

Figure S8. CV curves of MnO_2 and FLA-MnO_2 electrodes at different specific currents: (**a**) MnO_2, (**b**) FLA-MnO_2,

Figure S9

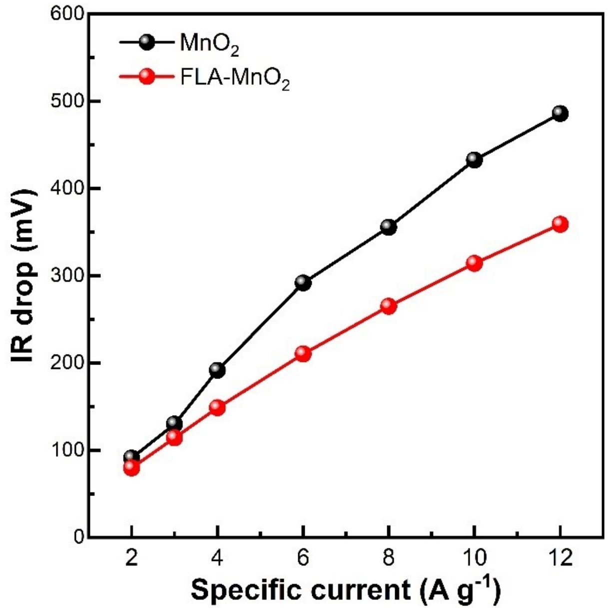

Figure S9. IR drop measured by the discharge curves at different specific currents.

Figure S10

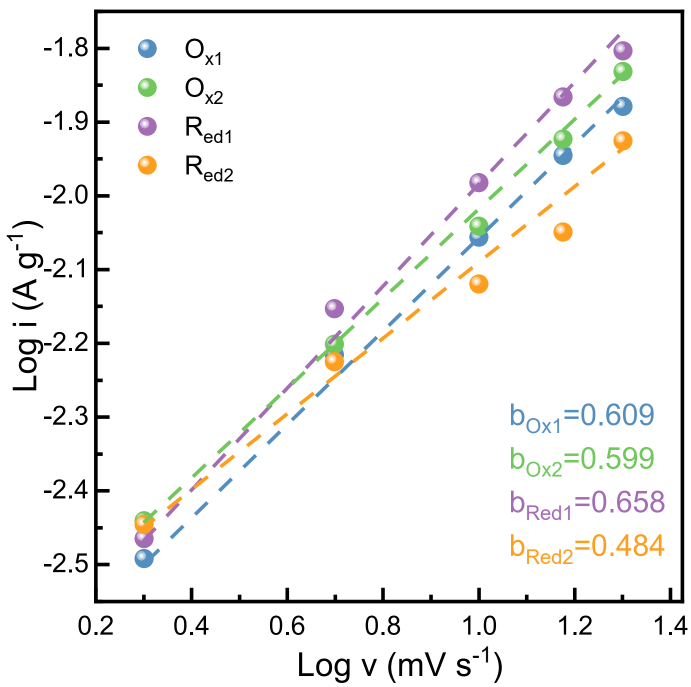

Figure S10. The relationship between peak current and scan rate in the logarithm (MnO_2).

Figure S11

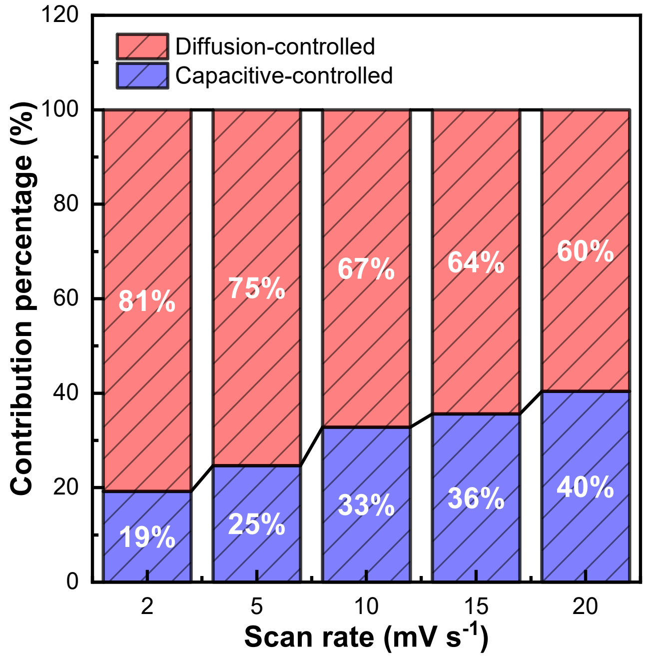

Figure S11. Diffusion-controlled and capacitive controlled contributions of MnO_2.

Figure S12

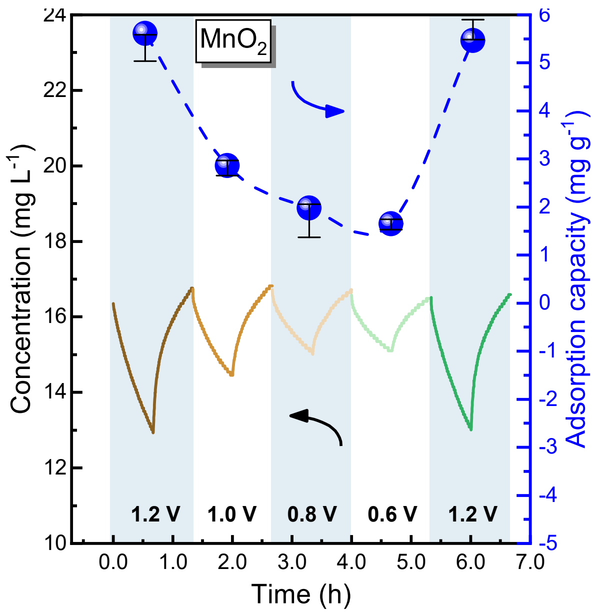

Figure S12. Plots of concentration versus time in HCDI cell with the MnO_2 electrode in 16.37 mg L^{-1} Li^+ ion solution at varying cell voltages and plots of adsorption capacity versus cell voltage (line with symbols).

Figure S13

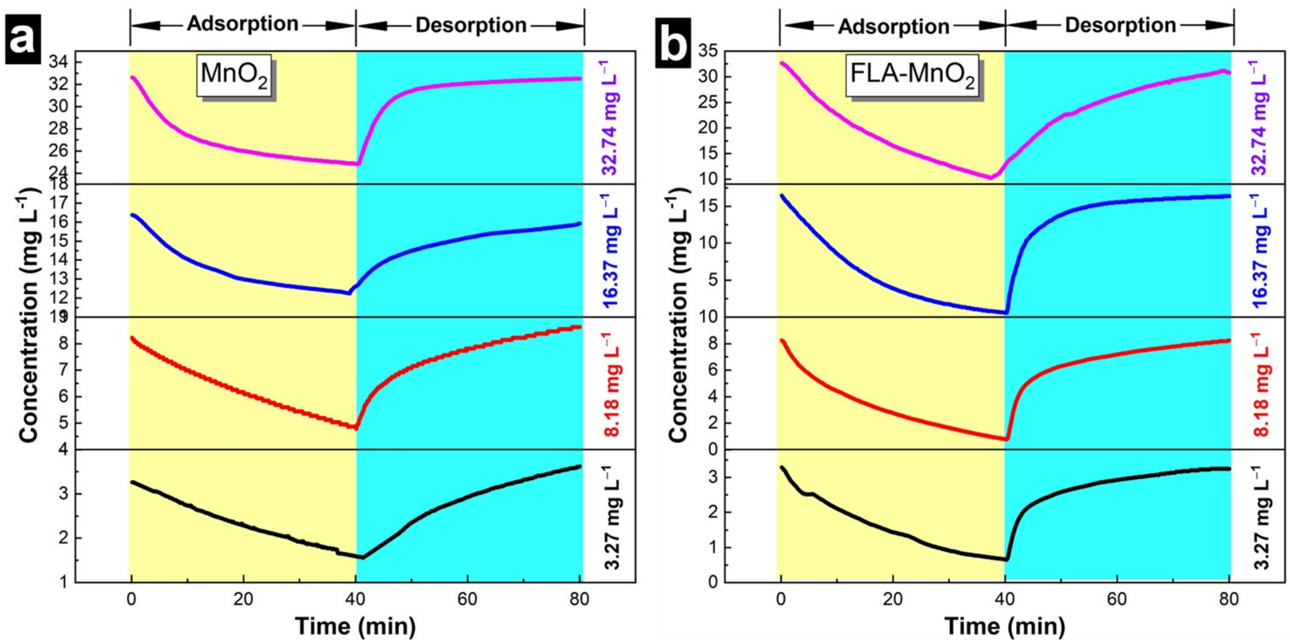

Figure S13. Plots of concentration versus time in HCDI cell with the MnO_2 and FLA-MnO_2 electrode at 1.2 V with varying feed concentrations.

Figure S14

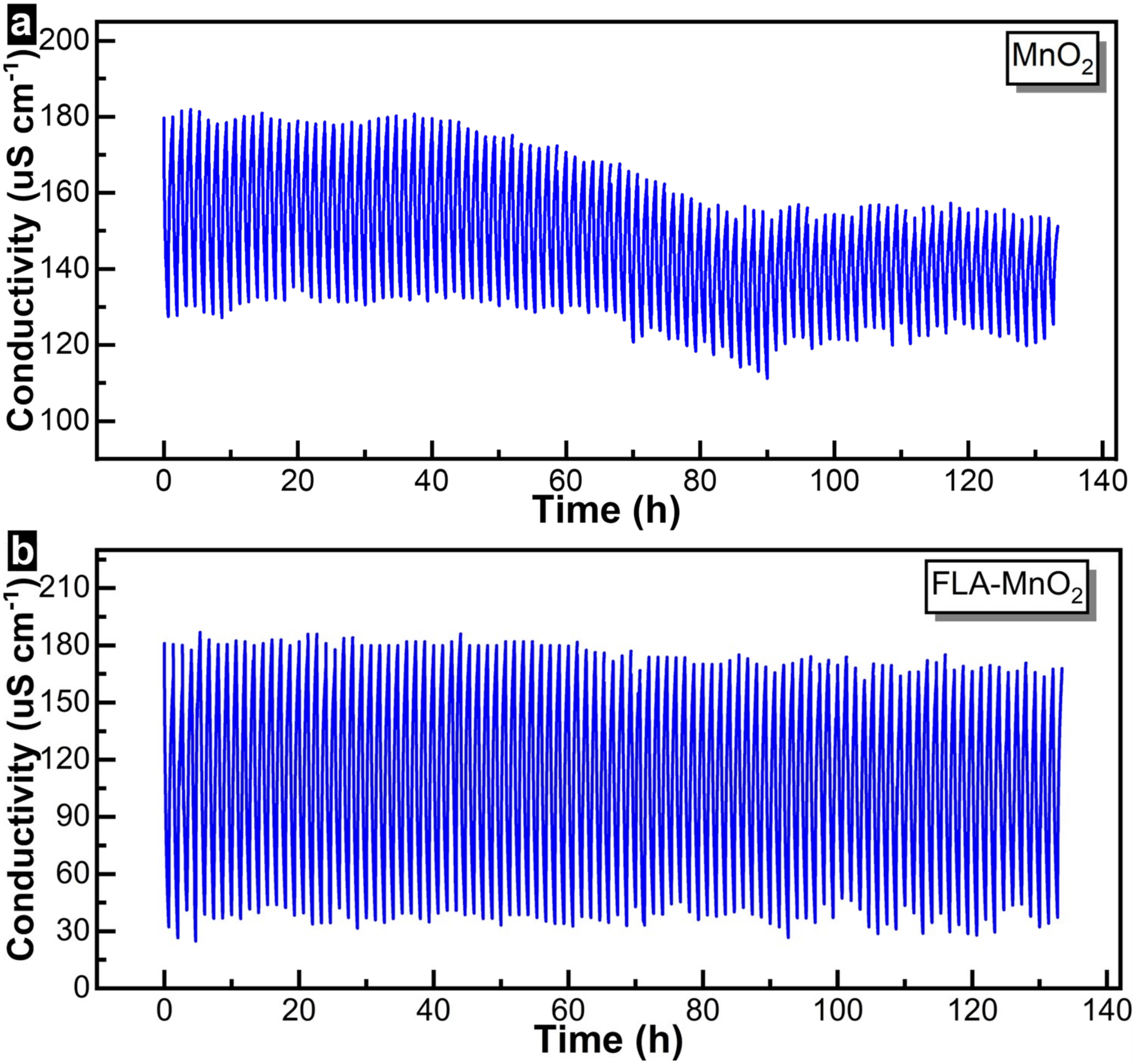

Figure S14. Conductivity curve during 100-time adsorption-desorption cycling test of (**a**) MnO_2, (**b**) FLA-MnO_2.

Figure S15

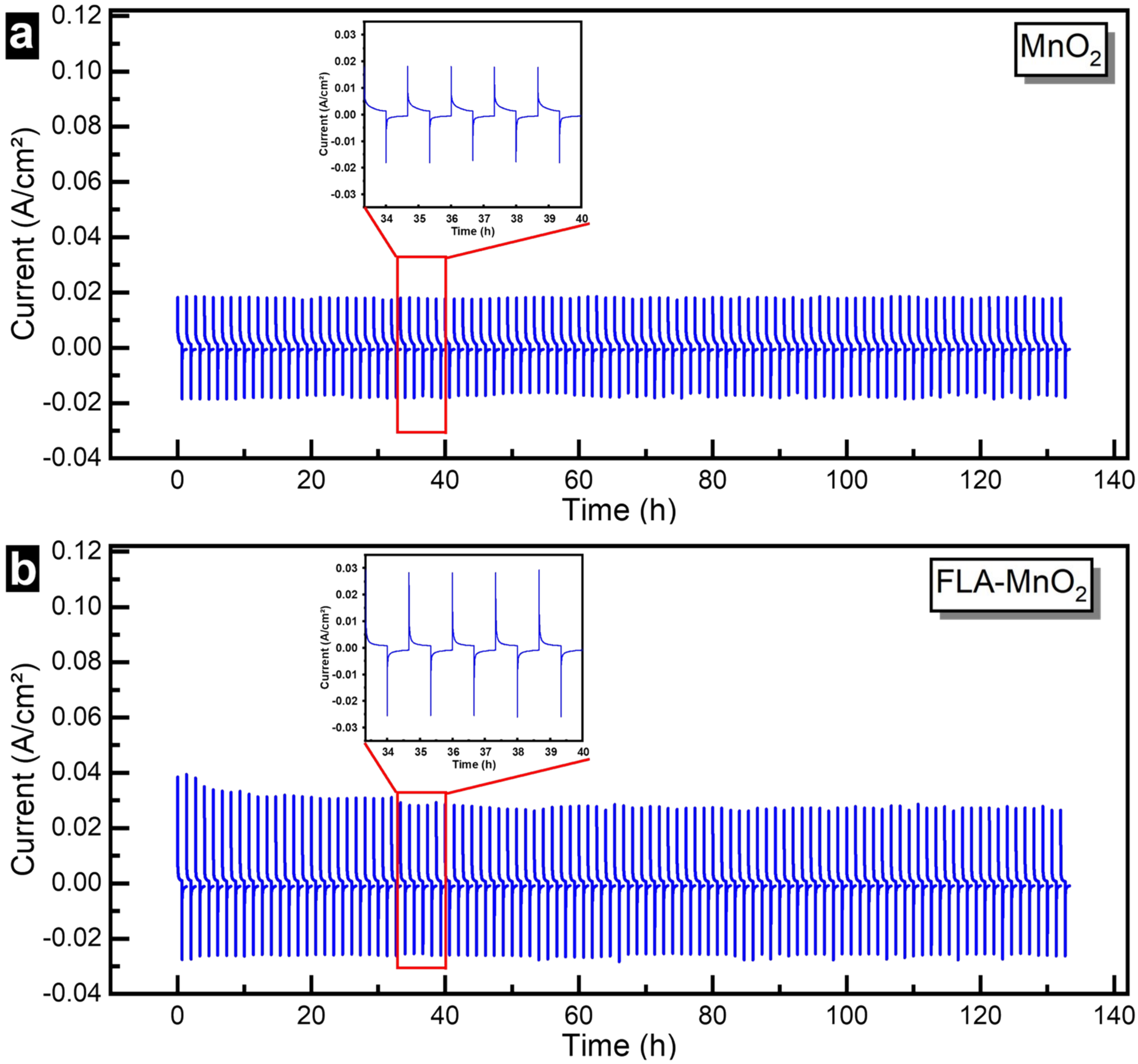

Figure S15. The current profile during 100-time adsorption-desorption cycling test of (**a**) MnO_2, (**b**) FLA-MnO_2.

Figure S16

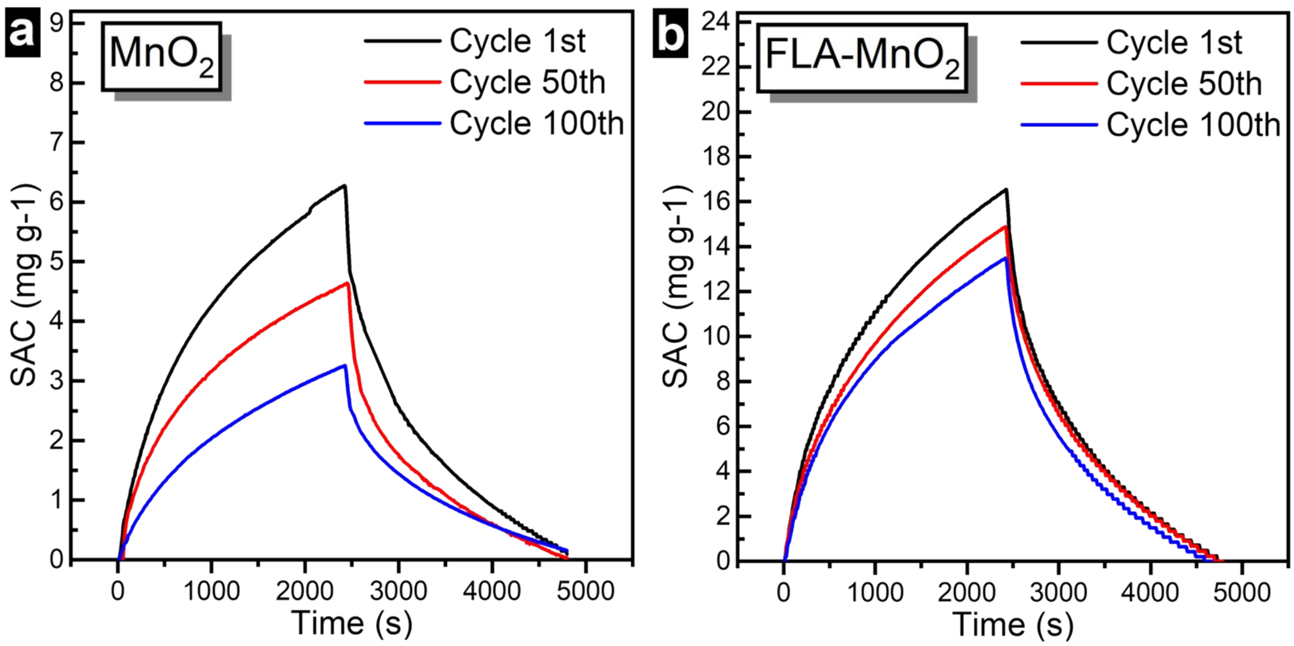

Figure S16. Electrosorption/desorption kinetics of (**a**) MnO_2, (**b**) FLA-MnO_2 at the Cycle 1st, 50th and 100th.

Figure S17

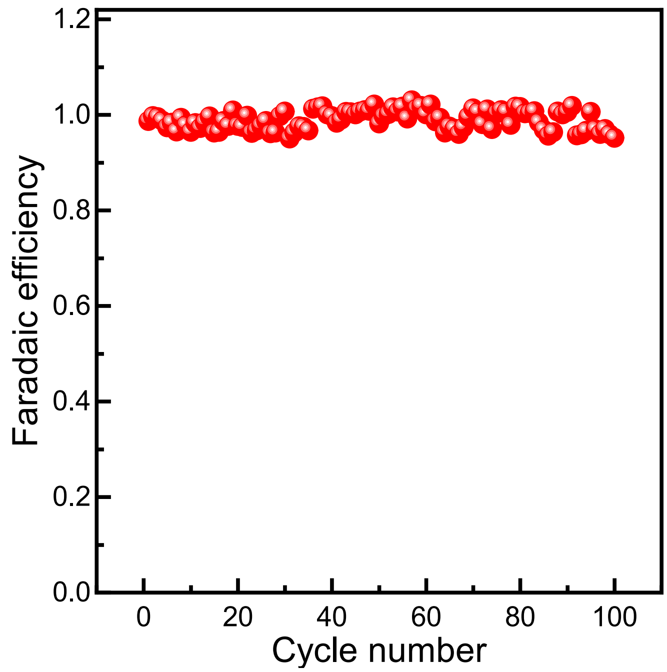

Figure S17. The effluent Faradaic efficiency for the FLA-MnO_2||AC cell during 100 cycles.

Figure S18

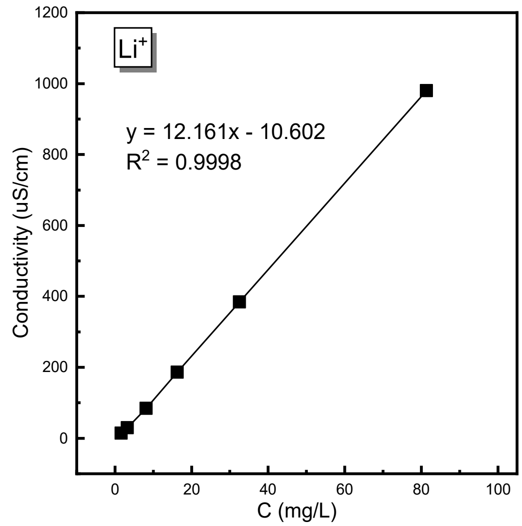

Figure S18. The correlation between the solutions with different Li^{+} concentrations prepared in the laboratory and the conductivity values obtained.

Supplementary References

[1] K. Zhang, M. Park, L. Zhou, G. H. Lee, J. Shin, Z. Hu, S. L. Chou, J. Chen, Y. M. Kang, Cobalt-Doped FeS_2Nanospheres with Complete Solid Solubility as a High-Performance Anode Material for Sodium-Ion Batteries, Angew. Chemie - Int. Ed. 55 (2016) 12822–12826. https://doi.org/10.1002/anie.201607469.

[2] S. Jia, J. Wei, B. Gong, Z. Shao, Sulfur vacancies enriched Nickel-Cobalt sulfides hollow spheres with high performance for All-Solid-State hybrid supercapacitor, J. Colloid Interface Sci. 601 (2021) 640–649. https://doi.org/10.1016/j.jcis.2021.05.127.

[3] Y. Bao, J. Hao, S. Zhang, D. Zhu, F. Li, Structural/Compositional-Tailoring of Nickel Hexacyanoferrate Electrodes for Highly Efficient Capacitive Deionization, Small 19 (2023) 1–11. https://doi.org/10.1002/smll.202300384.

[4] G. Tan, S. Wan, J.J. Chen, H.Q. Yu, Y. Yu, Reduced Lattice Constant in Al-Doped $LiMn_2O_4$ Nanoparticles for Boosted Electrochemical Lithium Extraction, Adv. Mater. 36 (2024) 1–10. https://doi.org/10.1002/adma.202310657.

[5] B. Hu, X. Shang, P. Nie, B. Zhang, J. Yang, J. Liu, Lithium ion sieve modified three-dimensional graphene electrode for selective extraction of lithium by capacitive deionization, J. Colloid Interface Sci. 612 (2022) 392–400. https://doi.org/10.1016/j.jcis.2021.12.181.

[6] N. Xie, Y. Li, Y. Yuan, J. Gong, X. Hu, Fabricating a Flow-Through Hybrid Capacitive Deionization Cell for Selective Recovery of Lithium Ions, ACS Appl. Energy Mater. 4 (2021) 13036–13043. https://doi.org/10.1021/acsaem.1c02654.

[7] Z. Zhang, X. Du, Q. Wang, F. Gao, T. Jin, X. Hao, P. Ma, J. Li, G. Guan, A scalable three-dimensional porous λ-MnO_2/rGO/Ca-alginate composite electroactive film with potential-responsive ion-pumping effect for selective recovery of lithium ions, Sep. Purif. Technol. 259 (2021) 118111. https://doi.org/10.1016/j.seppur.2020.118111.

[8] G. Ma, Y. Xu, A. Cai, H. Mao, X. Zhang, D.M. Shin, L. Wang, H. Zhou, Binder-Free $LiMn_2O_4$ Nanosheets on Carbon Cloth for Selective Lithium Extraction from Brine via Capacitive Deionization, Small 20 (2024) 1–12. https://doi.org/10.1002/smll.202306530.

[9] X. Zhao, M. Feng, Y. Jiao, Y. Zhang, Y. Wang, Z. Sha, Lithium extraction from brine in an ionic selective desalination battery, Desalination 481 (2020) 114360. https://doi.org/10.1016/j.desal.2020.114360.

[10] Y. Mu, C. Zhang, W. Zhang, Y. Wang, Electrochemical lithium recovery from brine with high Mg^{2+}/Li^+ ratio using mesoporous λ-MnO_2/$LiMn_2O_4$ modified 3D graphite felt electrodes, Desalination 511 (2021) 115112. https://doi.org/10.1016/j.desal.2021.115112.

[11] H. Kanoh, K. Ooi, Y. Miyai, S. Katoh, Electrochemical recovery of lithium ions in the aqueous phase, Sep. Sci. Technol. 28 (1993) 643–651. https://doi.org/10.1080/01496399308019512.

[12] X. Zhao, G. Li, M. Feng, Y. Wang, Semi-continuous electrochemical extraction of lithium from brine using CF-NMMO/AC asymmetric hybrid capacitors, Electrochim. Acta 331 (2020) 135285. https://doi.org/10.1016/j.electacta.2019.135285.

[13] W. Xu, L. He, Z. Zhao, Lithium extraction from high Mg/Li brine via electrochemical intercalation/de-intercalation system using LiMn2O4 materials, Desalination 503 (2021). https://doi.org/10.1016/j.desal.2021.114935.